Journal of Materials Chemistry A

ROYAL SOCIETY OF CHEMISTRY

PAPER

View Article Online
View Journal

Cite this: DOI: 10.1039/d5ta08099a

Regulating Ni oxidation states through ruthenium incorporation in Ni based catalysts

Laura Mallón,†[a] Laurent Peres,†[b] Nicolas Rivas,[c] Alba Garzón Manjón,‡[c] Cristina Scheu,[c] Marcos Gil-Sepulcre,[ad] Olaf Rüdiger,[d] Serena DeBeer,[d] Nuria Romero,[b] Jérôme Esvan,[e] Jordi García-Antón,[a] Luis Rodríguez-Santiago,[f] Xavier Solans-Monfort,[f] Roger Bofill,[a] Karine Philippot,*[b] Laia Francàs*[a] and Xavier Sala*[a]

NiFe-based materials are state-of-the-art electrocatalysts for water oxidation at alkaline pH. Several strategies to improve their activity have been reported, amongst which Ru-incorporation has appeared as a suitable approach. In this work, three Ni based nanomaterials have been prepared through organometallic synthesis and surface-decorated with small (sub-nanometric) Ru clusters (Ru(L)@Ni-NW) or large (*ca.* 8 nm) Ru nanoparticles (Ru(H)@Ni-NW and Ru(HH)@Ni-NW). As model systems, Ru(L)@Ni-NW and Ru(H)@Ni-NW have been thoroughly characterized by a complementary set of advanced techniques, including atom probe tomography, X-ray absorption spectroscopy, X-ray photoelectron spectroscopy and high-angle annular dark-field scanning transmission electron microscopy. Our study reveals that Ru nanoparticles remain unstable under electrocatalytic oxygen evolution reaction (OER) conditions, leaching from the Ni based NW surface. In contrast, sub-nanometric Ru clusters remain stable on the Ni based NWs and modify the Ni oxidation states at the surface sites, outperforming the counterparts that contain no Ru or Ru nanoparticles. The spectroelectrochemical and DFT modelling results suggest the interaction between the Ru sub-nanometric clusters and the Ni sites as the origin of the stabilization of Ni at higher oxidation states, boosting the OER efficiency under both Fe-containing (unpurified electrolyte) and Fe-free (purified electrolyte) conditions.

Received 3rd October 2025
Accepted 28th January 2026

DOI: 10.1039/d5ta08099a

rsc.li/materials-a

1. Introduction

Harnessing and storing solar energy in chemical bonds is a powerful alternative to current non-renewable and pollutant energy sources.[1] Amongst all the different possible strategies to achieve this objective, using green electricity to split water to generate H_2 (as a clean fuel) and O_2 is an attractive approach.[2,3] However, the extraction of four electrons and four protons from two water molecules to form an oxygen–oxygen double bond is a thermodynamically uphill and kinetically slow reaction, requiring the use of efficient catalysts.[4,5] Thus, from the anode perspective, the fine tuning of water oxidation catalysts to enhance their performance towards oxygen evolution is the cornerstone in the field. Fe-containing nickel-based materials are state-of-the-art electrocatalysts when performing water oxidation (OER) under basic conditions (pH 14). Over ten years, several studies demonstrated that the exceptional activity of Ni-based catalysts originates from the spontaneous incorporation of trace amounts of Fe from the electrolyte.[6–11] Since then, different studies have been devoted to understand the role of the incorporated Fe in the catalysis, increasing the conductivity,[6] acting as active species[7,8] or synergistically working with the Ni centers to evolve O_2.[9–11] However, this issue is still a subject of debate in the literature.[12–17] These studies also revealed that (1) there was a strong dependence of catalytic activity on the degree of Fe incorporation, with *ca.* 25% representing the optimal fraction;[7] (2) the regulation of the Ni(III/II) redox potential was clearly observed, with Ni(II) being more stable after Fe incorporation.[6,18,19]

[a]*Departament de Química, Unitat de Química Inorgànica, Universitat Autònoma de Barcelona, Cerdanyola del Vallès, 08193 Barcelona, Spain. E-mail: laia.francas@uab.cat; xavier.sala@uab.cat*

[b]*CNRS, LCC (Laboratoire de Chimie de Coordination), UPR8241, University of Toulouse, UPS, INPT, Toulouse, Cedex 4 F-31077, France. E-mail: karine.philippot@lcc-toulouse.fr*

[c]*Max Planck Institute for Sustainable Materials GmbH, Max-Planck-Str. 1, 40237 Düsseldorf, Germany*

[d]*Max Planck Institute for Chemical Energy Conversion, Stiftstrasse 34-36, D-45470 Mülheim an der Ruhr, Germany*

[e]*Institut Carnot – Centre Inter-universitaire de Recherche et d'Ingénierie des Matériaux, INP-ENSIACET, CNRS, Université de Toulouse, 118, route de Narbonne, 31062 Toulouse, France*

[f]*Departament de Química, Universitat Autònoma de Barcelona, Cerdanyola del Vallès, 08193 Barcelona, Spain*

† Equal contribution.

‡ Current address: Catalan Institute of Nanoscience and Nanotechnology (ICN2), CSIC and BIST, Campus UAB, Bellaterra, 08193 Barcelona, Catalonia, Spain.

Among the different strategies that have been used to further increase the activity of Ni-based catalysts,[20] the incorporation of metal elements has been shown to be a promising route.[21–24] Several studies confirmed the improvement of the electrocatalytic water oxidation activity of Ni-based nanomaterials by Ru incorporation *via* both atomically distributed Ru (single atoms)[21,22,25] or Ru/RuO_2 nanoparticles (NPs) (Table S1).[23,26] The high OER activity reported when incorporating RuO_2 NPs has been widely attributed to synergistic effects between Ru and Ni. It has been reported that at a RuO_2/NiO(OH) interface,[26] dissociation of both H_2O and OH^- (which is not optimal in NiO(OH) or in RuO_2 separately) can be coupled and optimized to produce the ^-OOH intermediate, which can be further deprotonated to release O_2. This has been attributed to the ability of NiO(OH) to favour the dissociation of water molecules[27] and that of RuO_2 to dissociate OH^- moieties.[28,29] It has also been reported that Ru can aid the electron transfer process between the water substrate and the intermediate species, facilitating O–O bond formation at basic pH.[23] On the other hand, when dispersed single atoms are incorporated into Ni-based catalysts, a change in the electronic structure of the resulting catalysts is detected.[21,22,25] In all these studies, DFT calculations reveal a change in the Ni d band position, thus provoking the optimization of the adsorption energy of intermediate species. In addition, a recent report has related the incorporation of Ru single atoms into Ni-based catalysts with the stabilization of Ni high oxidation states and dynamic surface reconstruction.[25] All these studies demonstrate that the effect of incorporated Ru depends on its size and morphology, with Ru ranging from single atoms to nanoparticles, influencing Ni-based catalysts in different ways, from directly promoting O–O bond formation to modulating oxidation states and the electronic structure. However, despite the number of reports devoted to the effect of Ru incorporation on the OER performance of Ni-based electrocatalysts, no study has yet compared the effect of Ru species of different sizes and morphologies (*i.e.*, clusters and NPs) on a single Ni-based substrate. Different Ru morphologies, from single atoms to clusters or NPs, can interact with the Ni host in fundamentally distinct ways, potentially altering the electronic structure, oxidation states and the adsorption energies of reaction intermediates, or determining the stability of the hybrid materials under electrocatalytic turnover. The thorough structural and electronic characterization of the interface of different morphologies of incorporated Ru species within a given Ni-based material is thus of particular interest to unravel the structure–function relationships that govern OER efficiency and enable the rational design of improved OER electrocatalysts.

In this work, we report the synthesis of three Ru-incorporating Ni-based nanomaterials that consist of Ni-based nanoworms (NWs) post-functionalized with three different amounts of Ru (0.4 wt%, 3.2 wt% and 6.4 wt%), which have been prepared through the organometallic synthetic method,[30] allowing a fine control of the nanostructure (Ni NWs, Ru NPs or subnanometric Ru clusters) and surface composition. The nanomaterials containing 0.4 and 3.2 wt% Ru have been fully characterized by a complementary set of advanced microscopy and spectroscopic techniques, revealing that Ru is present as small (sub-nanometric) clusters finely distributed throughout all the Ni based surface in the low Ru containing material, while *ca.* 8 nm NPs are present in the high Ru containing one. The 6.4 wt% Ru containing nanomaterial was not fully characterized due to the similar Ru NP structure formed in the 3.2 wt% system. When the two selected nanomaterials are tested for the electrochemical OER under alkaline conditions, the low Ru incorporating Ni-based electrocatalyst outperforms both the non-incorporating and the high Ru-incorporating counterparts. The reasons behind this superior performance are discussed in view of the structural and electronic features of the synthesized nanomaterials. Our results highlight the importance of tuning the size and nature of the incorporated Ru to modulate the interaction with the Ni catalyst, adjusting the influence of the incorporated metal on the Ni electronic structure and enhancing the resulting OER performance.

2. Experimental section

2.1. Reagents

All procedures concerning the synthesis and preparation of samples were carried out using standard Schlenk tubes, Fisher-Porter glassware and vacuum line techniques or with the use of a glove-box (MBraun) under an argon atmosphere. Tetrahydrofuran (THF) was obtained from Carlo Erba, purified using purification MBraun SPS-800 equipment and degassed with three freeze–pump–thaw cycles before use. Absolute anhydrous ethanol (Carlo Erba, ACS reagent) was dried over a molecular sieve and degassed by Ar bubbling before use. Bis(1,5-cyclooctadiene) nickel(0) [$Ni(COD)_2$] (>98%, Strem Chemicals) and [Ru(Me-allyl)$_2$(COD)] (Sigma-Aldrich) were stored under argon inside a glovebox (MBraun). Deionized water was obtained from Millipore (MilliQ, 18.2 MΩ cm^{-1}; Millipore, Bedford, MA). Ar and H_2 were purchased from Air Liquide (Alphagaz).

2.2. Synthetic procedures

2.2.1. Synthesis of Ni nanoworms (Ni-NWs).[31] Under an argon atmosphere, $Ni(COD)_2$ (4.0 mmol, 1.1 g) was added into a Fischer–Porter tube and solubilized in THF (180 mL). Then, outside the glovebox, ethanol (20 mL, 10% v/v) was added with a syringe under Ar. The Fischer–Porter tube was then pressurized with 3 bar of hydrogen and the reaction mixture was kept at 70 °C under vigorous stirring for 20 h. Then, excess H_2 was evacuated and the solvent was evaporated under vacuum. The product was collected inside the glovebox using a magnet and by scraping with a spatula and stored under an inert atmosphere in a closed vial.

2.2.2. Synthesis of Ru(L)@Ni-NW, Ru(H)@Ni-NW and Ru(HH)@Ni-NW. Under an argon atmosphere, three different amounts (1, 5 and 10 wt%, theoretical values) of [Ru(Me-allyl)$_2$(COD)] were added to a Fischer–Porter tube containing a dispersion of the pre-synthesized Ni NWs in THF, and the reaction mixtures were vigorously stirred for 3 days at room temperature to optimize the impregnation of the Ru precursor on the Ni NWs. Next, the reaction vessels were pressurized with

3 bar of H_2 at 50 °C for 18 h to reduce the Ru complex. The remaining H_2 was removed under vacuum and the application of a magnet on the reactor walls allowed separation of a black powder that was washed with THF (×3) and pentane (×3). The resulting black powder was dried under vacuum and collected in a vial. The collected powder was passivated under slow atmospheric air diffusion inside the closed vial for 3 weeks.

2.3. Characterization techniques

Transmission electron microscopy (TEM) and high resolution transmission electron microscopy (HRTEM) analyses were performed at the "Centre de microcaractérisation Raimond Castaing, CNRS UAR 3623, Toulouse" by using a JEOL JEM 1400 operating at 120 kV with a point resolution of 2.0 Å. High resolution analyses were conducted using a JEOL JEM 2100F equipped with a Field Emission Gun (FEG) operating at 200 kV with a point resolution of 2.3 Å and a JEOL JEM-ARM200F Cold FEG (cold field emission gun) operating at 200 kV with a point resolution of 1.9 Å and coupled to an EDX spectrometer and an electron energy loss spectrometer (EELS).

2.3.1. Scanning electron microscopy (SEM). SEM observations were conducted on a JEOL 6700F microscope at the "Centre de microcaractérisation Raimond Castaing, CNRS UAR 3623, Toulouse".

2.3.2. HAADF-STEM. We conducted the scanning transmission electron microscopy (STEM) analyses utilizing a Cs-corrected Titan Themis 60-300 X-FEG microscope. The microscope was equipped with a high-angle annular dark-field (HAADF) detector ranging from 73 to 352 mrad and a camera length of 48 mm. Additionally, we employed energy dispersive X-ray (EDX) chemical mapping. To optimize the microscope, we set the convergence semi-angle at approximately 23.8 mrad, the beam size at around 0.1 nm, and the current at approximately 150 pA.

2.3.3. Atomic probe tomography (APT). For APT measurements, all samples were embedded in a Co matrix and deposited on Cu foil following the co-deposition procedure described by Kim *et al.*[32] Co was chosen as the embedding matrix due to its similar evaporation field (37 V nm^{-1}) to Ni (35 V nm^{-1}) and Ru (41 V nm^{-1}). This reduces the chromatic aberrations originating from the field evaporation process. Moreover, it facilitates mass spectral analysis, since it only has one isotope, and it considerably reduces the probability of peak overlaps. APT needles were subsequently prepared with the use of a focused ion beam (Dual Beam, Thermo Fisher Scientific Helios 600) microscope. Finally, APT measurements were carried out on a CAMECA LEAP 5000XR system where the specimens were kept at 50 K. Measurements were performed in pulsed laser mode (UV laser: wavelength = 355 nm) with 60 pJ laser energy and a pulse frequency of 125 kHz, while keeping the detection rate at 1 ion for every 200 pulses. Data analysis and visualization were carried out with the AP Suite 6.2 software (CAMECA instruments) following the tip profile reconstruction protocol.

2.3.4. X-ray photoelectron spectroscopy (XPS). The XPS spectra were collected using a Thermo Scientific K-Alpha system using a monochromatized Al K-alpha ($h\nu$ = 1486.6 eV) source (CIRIMAT Toulouse). The size of the X-ray spot was about 400 μm. The pass energy was respectively fixed at 30 eV for core levels (step 0.1 eV) and 160 eV for surveys (step 1 eV). The Au $4f_{7/2}$ (83.9 ± 0.1 eV) and Cu $2p_{3/2}$ (932.8 ± 0.1 eV) photoelectron lines were used to calibrate the spectrometer energy. All the XPS spectra were collected in direct mode N (Ec), coupled with subtraction of the background signal *via* the Shirley method. The charge effect was neutralized by using a flood gun on the top surface. The XPS measurements of the samples after activation were carried out at the Catalan Institute of Nanoscience and Nanotechnology (ICN2) in Barcelona with a Phoibos 150 analyzer (SPECS GmbH, Berlin, Germany) under ultra-high vacuum conditions (base pressure 5–10 mbar) with a monochromatic aluminium K-alpha X-ray source (1486.74 eV) on the catalysts deposited onto FTO to be used as an electrode.

2.3.5. Powder X-ray diffraction (PXRD). The crystallinity and phase purity of the samples were investigated by XRD on a Panalytical MPDPro diffractometer using Cu Kα radiation (λ = 1.5418 Å) at LCC-CNRS Toulouse.

2.3.6. Inductively coupled plasma optical emission spectroscopy (ICP-OES). Ru contents were determined by ICP-OES using a PerkinElmer Optima 2100 DV instrument at LCC-CNRS Toulouse.

2.3.7. X-ray absorption spectroscopy. Ni and Ru K-edges were used to measure Ni-NWs, Ru(L)@NiNW and Ru(H)@Ni-NW, and the reference samples Ni(0), Ru(0) and RuO_2 in transmission mode. All samples were prepared by diluting the corresponding powder sample with cellulose in a pellet (φ = 6 mm). Afterwards, the samples were placed in a sample holder and sealed with 30 μm Kapton tape. Measurements were carried out at beamline CLAESS (Static Ni/Ru K-edge XAS and EXAFS) at ALBA synchrotron with the collaboration of the beamline scientist and ALBA staff. The incident energy was selected using a Si (311) double crystal monochromator. Incident flux was *ca.* 5 × 10^{11} ph sec^{-1} using a beam size of 150 μm × 150 μm. Samples were kept below 80 K in a N_2 LN_2-cryo cryostat. Incident energy was calibrated by assigning the inflection point of Ru and Ni foil to 22 117 and 8333 eV, respectively. A step size of 0.2 eV was used in the XANES and EXAFS regions (1 s integration time). Final spectra were processed and normalized using the Athena program, included in the DEMETER package.[33]

2.3.8. Electrochemical measurements. Electrocatalytic experiments were performed at room temperature at pH 14 (1 M NaOH) in a three-electrode configuration using a saturated calomel electrode and Pt as reference and counter electrodes, respectively. A GC-RDE ($\varnothing$ = 0.3 cm, S = 0.07 cm^2) was used as a working electrode (WE) after drop-casting each sample from a THF suspension (2 mg mL^{-1}). The potential was controlled using a BioLogic SP-150 potentiostat and the EC-Lab software for data acquisition and data handling. IR drop was automatically corrected at 85% for cyclic voltammetry and chronoamperometry measurements. All catalytic experiments were conducted with a sweep rate of 10 mV s^{-1}. Potentials are reported *vs.* RHE (E_{RHE} = E_{SCE} + 0.244 V + (0.059 × pH)) and overpotentials are calculated as η_0 = E_{SCE} + 0.244 V − (1.23–0.059 × pH). The systems were scanned from −0.25 V to 1.25 V *vs.* RHE at 100 mV s^{-1} and the controlled potential chronoamperometric experiments were performed at E_{app} = 1 V *vs.* RHE. A purified 1 M NaOH electrolyte (*i.e.*

Fe-free) was prepared following a procedure reported by Trotochaud *et al.* to compare its effect with the as-prepared (non-purified) 1 M NaOH electrolyte.[13]

2.3.9. TOF calculation. To estimate the TOF of the OER process, the amount of electroactive $Ni(OH)_2$ species in each sample was extracted from the integration of the total charge under the $Ni(OH)_2$/NiOOH oxidation wave *ca.* 1.5 V *vs.* RHE, considering that this is a one electron oxidation process. Afterwards, the intensity of each CV was divided by the charge of the $Ni(OH)_2$/NiOOH oxidation wave to obtain the corresponding CV normalized by the TOF.

2.3.10. *In situ* UV-vis spectroelectrochemistry. UV-vis spectra were collected using a Cary 60 UV-vis spectrometer (Agilent Technologies) at the UAB. Spectra were collected between 290 and 900 nm with a medium scan rate. Electrochemical experiments were carried out using a PalmSens4 potentiostat in a typical three-electrode configuration by using Ag/AgCl (KCl saturated) and Pt mesh as reference and counter electrodes, respectively. The WE was prepared by drop-casting 2 drops of 25 μL of a suspension of the material in THF (2 mg mL^{-1}) onto a fluorine doped tin oxide (FTO) electrode (Xop Física, $S = 1$ cm^2). All potentials are reported *versus* the reversible hydrogen electrode ($E_{RHE} = E_{Ag/AgCl} + E^0_{Ag/AgCl} + 0.059\,V \times pH$), where $E^0_{Ag/AgCl} = 0.199$ V. The electrodes were cleaned prior to the measurements in high purity ethanol and afterward rinsed with Milli-Q water using sonication. A 1 M NaOH aqueous solution (pH ∼ 14) was used as the electrolyte in all experiments, unless otherwise stated.

2.4. Computational details

2.4.1. Models. The models were built from the β-phase of $Ni(OH)_2$ (see Fig. 8), which consists of a one layer (6 × 6) supercell slab of the (001) surface. Periodic boundary conditions were applied in all directions with a vacuum space of at least 20 Å in the direction perpendicular to the surface to eliminate spurious image–image interactions. Three types of Ru clusters were added on the surface, one consisting of pure metallic Ru with 10 atoms (Ru_{10}) constructed from two close-packed planes and two RuO_X clusters with different degrees of oxidation ($Ru_{17}O_{15}$ and $Ru_{17}O_{27}$). The RuO_X clusters were constructed from the Wulff-like $(RuO_2)_{24}$ nanoparticles constructed with the BCN-M computational tool.[34] They are based on two layers of RuO_2 in which all dangling O atoms in $Ru_{17}O_{27}$ and most of the mono- and decoordinated O atoms in $Ru_{17}O_{15}$ were removed. Remarkably, several protons of the $Ni(OH)_2$ surface were removed to accommodate these doping clusters and allow the interaction of their ruthenium centers with the oxygen atoms of $Ni(OH)_2$. Finally, we ensured that the computed trends do not depend on the incorporation of iron. For this reason, a fourth model was constructed in which one Ni center is substituted by Fe in the slab containing the $Ru_{17}O_{27}$ cluster.

For each model, different types of OH groups of the $Ni(OH)_2$ surface were identified as a function of the distance from and position of the Ru clusters. For these different H atoms of $Ni(OH)_2$, the feasibility of their oxidation was evaluated through a proton coupled electron transfer (PCET) process described as

$$*OH \rightarrow *O + H^+ + 1e^- \quad (1)$$

2.4.2. Level of theory. All calculations were performed with the PBE density functional[35] as implemented in the VASP.[36,37] The Hubbard-like term (U) was used, as defined by Dudarev *et al.*,[38] to account for the strong correlation in the 3d orbitals of Ni. The U value was fixed to 5.5 eV as suggested in previous contributions.[39] Moreover, dispersion forces were described with Grimme's D3 empirical correction (PBE-D3 + U).[40] Atomic cores are described with PAW pseudopotentials[41,42] and the valence electrons are represented with a plane-wave basis set with an energy cutoff of 500 eV. A (2,2,1) Monkhorst–Pack K-point mesh was employed to sample the first Brillouin zone. The energy convergence criteria are fixed at 10^{-5} and 10^{-4} eV for electronic and geometry relaxations, respectively. This methodology was previously used in the modeling of other Ru-based materials for the HER[43,44] and IrO_2 nanoparticles and their electrocatalytic activity.[45,46] Solvation effects were included by using the implicit model implemented in VASPsol[47] through single point calculations at vacuum optimized geometries. Thermal corrections at 1 atm and $T = 273$ K were added considering the contributions of the normal modes associated with the adsorbed species.

The ΔG^0 values for the PCET step described in eqn (1) were computed by using the computational standard hydrogen electrode as defined by Rossmeisl, Nørskov and co-workers, which allows replacing a proton and an electron with half a hydrogen molecule at $U = 0$ V *vs.* SHE.[48] Then, under standard conditions, the free energy of the reaction (eqn (1)) can be calculated as the free energy of

$$*OH \rightarrow *O + \tfrac{1}{2}H_2 \quad (2)$$

For this reaction, ΔG^0 can be approximated as ΔG at $U = 0$, pH = 0, $P = 1$ bar and $T = 298.15$ K. Thus, $\Delta G^0 = \Delta E + \Delta ZPE - T\Delta S$, where ΔE is calculated using DFT and vZPE and ΔS were calculated using the DFT computed vibrational frequencies. Entropy contributions for H_2 were obtained from the tabulated values. At a pH different from 0 the free energy of the H^+ ions can be corrected by considering the concentration dependence: $\Delta G_{pH}(pH) = -kT \ln[H^+]$. Thus, the free energy of the reaction is calculated as

$$\Delta G^0(pH) = \Delta G^0(pH = 0) + \Delta G_{pH}(pH) \quad (3)$$

3. Results and discussion

3.1. Synthesis of the Ru-incorporating Ni-based nanomaterials

The Ru-incorporating Ni-based nanomaterials were synthesized by an organometallic approach[30] following a two-step procedure (Scheme 1). First, nickel nanoworms (Ni-NWs) were produced by hydrogenation of the [Ni(COD)$_2$] complex (COD = 1,5-cyclooctadiene), in ethanol/THF (10% v/v), under 3 bar of H_2 at 70 °C, as previously reported.[31] These Ni-NWs are made of

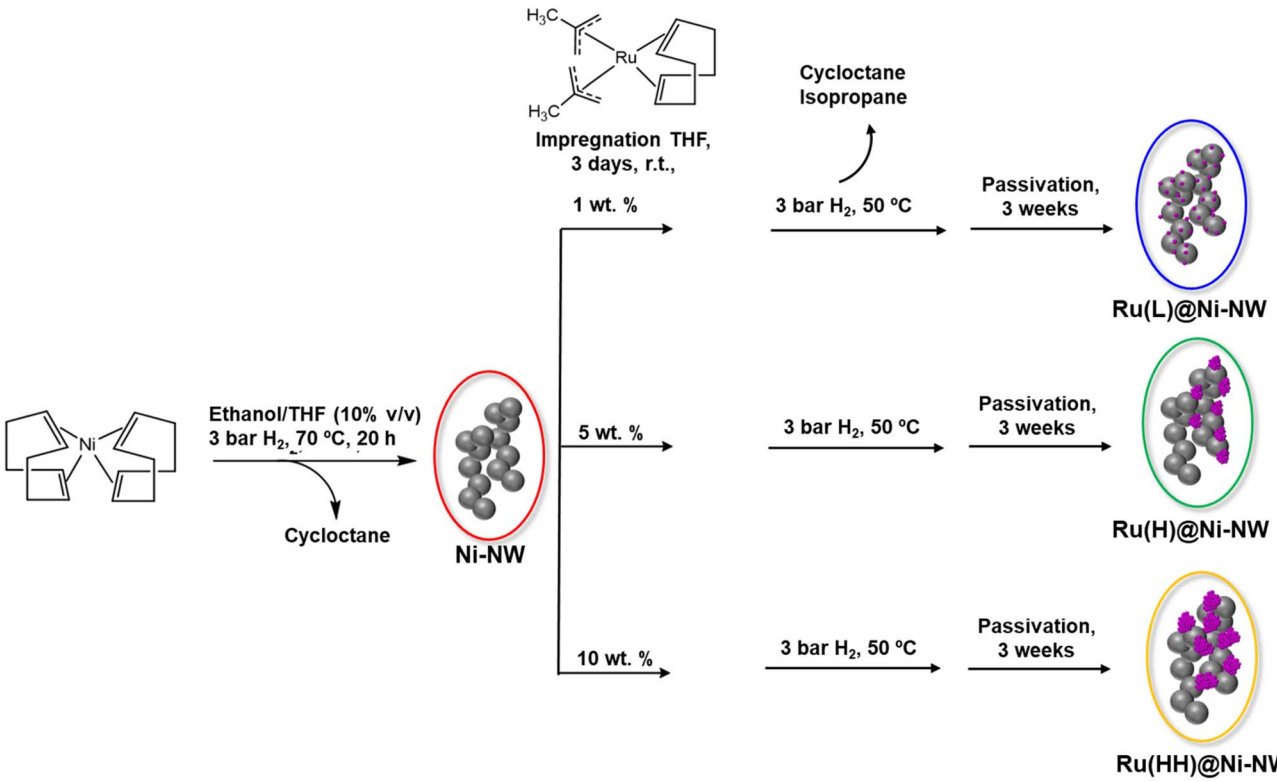

Scheme 1 Organometallic synthesis of pristine Ni-NWs and three Ru@Ni-NW nanomaterials.

agglomerated Ni NPs, which provide a porous structure to the Ni-based nanomaterial.[31] Second, Ru incorporation was performed on top of the pre-synthesized Ni-NWs by reduction of the [Ru(Me-allyl)$_2$(COD)] (Me-allyl = 2-methylallyl) complex as a Ru source. In this second step, the pre-synthesized Ni-NWs were first mixed with a THF solution of the Ru precursor for 3 days at room temperature under vigorous stirring to ensure the impregnation of the precursor all over the Ni-NW nanomaterials. Then, the Ru-impregnated Ni-NW nanomaterials were exposed to 3 bar of H_2 at 50 °C to induce the reduction of the Ru precursor (Fig. 1). For comparative purposes, the Ru impregnation was performed at three different Ru loadings (1, 5 and 10 wt%, theoretical values), yielding three Ru-incorporating nanomaterials, the one corresponding to low (L) Ru content, Ru(L)@Ni-NW, the one corresponding to the high (H) Ru content (5%), Ru(H)@Ni-NW, and the one corresponding to very high (HH) Ru content (10%), Ru(HH)@Ni-NW, respectively. All nanomaterials were allowed to passivate under slow atmospheric air diffusion inside a closed vial for 3 weeks before running the electrocatalytic tests. This passivation step ensured homogeneous and comparable catalysts by minimizing variations in air exposure that could modify the active surface and compromise reproducibility in OER measurements. The latter is a key parameter when studying catalytic processes.

3.2. Structural characterization of Ni-NWs, Ru(L)@Ni-NW and Ru(H)@Ni-NW

State-of-the-art techniques such as transmission electron microscopy (TEM), scanning electron microscopy (SEM), high-angle annular dark-field scanning transmission electron microscopy coupled with energy dispersive X-ray spectroscopy (HAADF-STEM- EDX), powder X-ray diffraction (PXRD), inductively coupled plasma optical emission spectroscopy (ICP-OES), X-ray photoelectron spectroscopy (XPS), atomic probe tomography (APT) and X-ray absorption spectroscopy (XAS) were used to structurally and chemically characterize the Ni-NW, Ru(L)@Ni-NW and Ru(H)@Ni-NW nanomaterials. For Ru(HH)@Ni-NW only TEM and SEM characterization was performed due to the encountered similarity to Ru(H)@Ni-NW.

3.2.1. Electron microscopy characterization: TEM, HAADF-STEM and SEM. TEM and SEM images of Ni-NWs revealed the presence of nanoworms composed of large Ni-based particles of *ca.* 100 nm in size that result from the agglomeration of smaller nanoparticles of *ca.* 22 nm in size (Fig. 1a and b). These images also indicate the foam-like character of this Ni nanomaterial, suggesting its porous nature, as previously reported.[31] The TEM and SEM analyses of the three Ru-incorporating Ni-NW nanomaterials also showed the presence of worm-like superstructures made of particles as for the initial Ni-NW nanomaterial, which served as a support for the growth of the Ru species in the second step of the synthesis (Scheme 1 and Fig. 1). In the TEM images recorded for Ru(L)@Ni-NW, there is no clear evidence of the formation of Ru NPs over the Ni-NWs (Fig. 1c). However, EDX analysis (Fig. 1e) confirmed the presence of both Ni and Ru, attesting that the Ru deposition occurred well onto the Ni-NWs. This result, together with the absence of visible Ru dots attributable to Ru NPs on the Ni-NWs in the TEM analysis, suggests that the Ru has been deposited as small clusters or

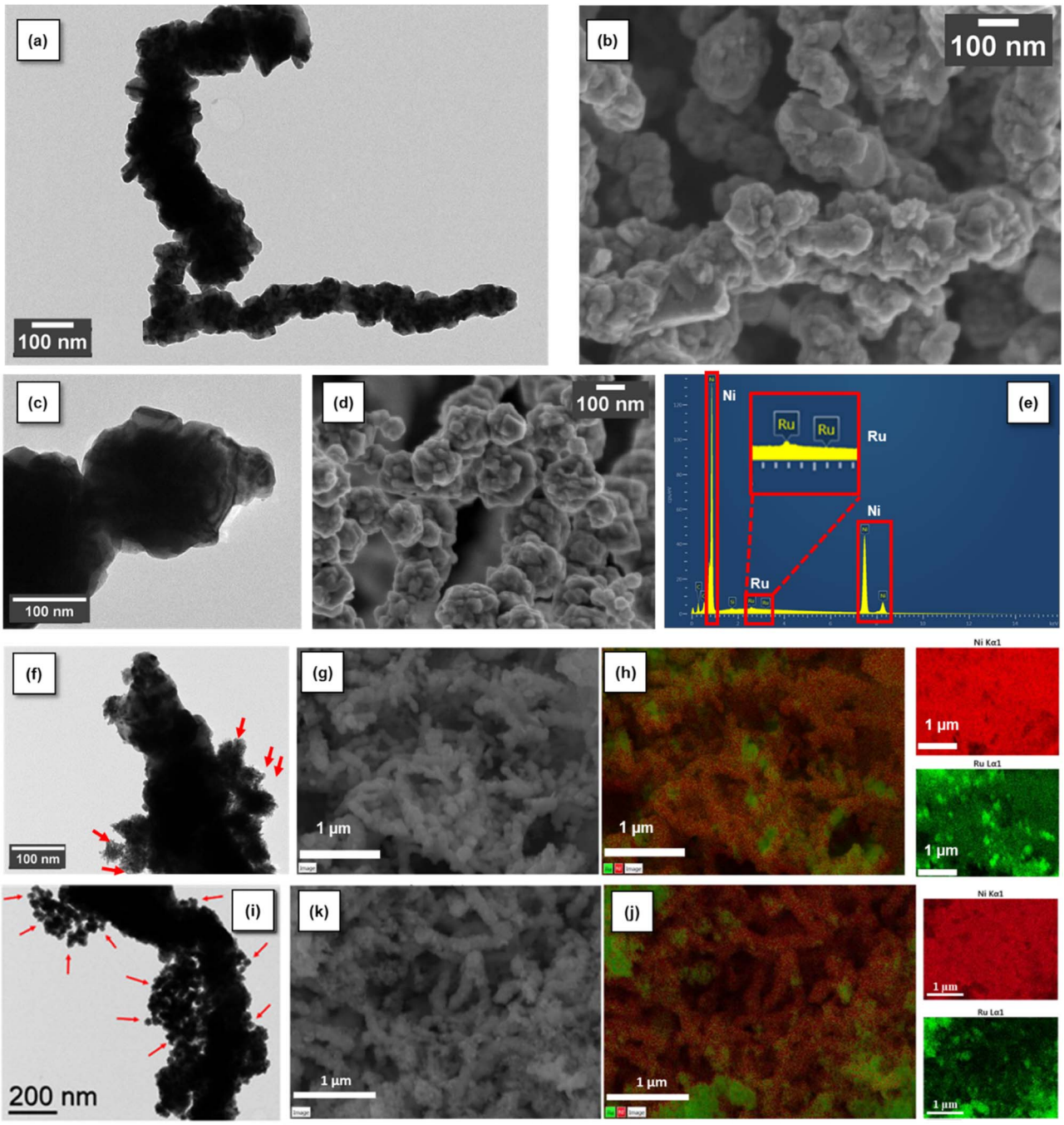

Fig. 1 From top to bottom: Ni-NW characterization by TEM (a) and SEM (b); Ru(L)@Ni-NW characterization by TEM (c), SEM (d) and EDX analysis (e); Ru(H)@Ni-NW characterization by TEM (f), SEM (g) and EDX mapping of Ni Kα1 (red) and Ru Lα1 (green) (h); Ru(HH)@Ni-NW characterization by TEM (i), SEM (j) and EDX mapping of Ni Kα1 (red) and Ru Lα1 (green) (k). The arrows in (f) and (i) show the presence of small Ru NPs.

single atoms onto the Ni-NW nanomaterial. In contrast, the TEM (Fig. 1f and i) and SEM (Fig. 1g and j) images and the EDX mapping (Fig. 1h and k) of Ru(H)@Ni-NW and Ru(HH)@Ni-NW, respectively, revealed the presence of Ru NPs on the Ni-NWs. For Ru(H)@Ni-NW this was further confirmed by PXRD and APT (see Sections 2.2.2 and 2.2.4). Due to the presence of the same Ru NPs in both Ru(H)@Ni-NW and Ru(HH)@Ni-NW and their similar electrochemical behavior (see Fig. S1 and 5c), Ru(H)@Ni-NW was selected to study the effect of incorporating Ru in the form of NPs onto Ni-NWs. The Ru(HH)@Ni-NW nanomaterial was not studied further.

The HAADF-STEM analysis of Ni-NWs, Ru(L)@Ni-NW and Ru(H)@Ni-NW (Fig. S2) confirmed the TEM results. The quantity of the Ru precursor mixed with the Ni-NWs appeared to have a direct impact on the structural characteristics and arrangement of the Ru atoms within the Ni-NWs. Thus, while the HAADF-STEM analysis of the Ru-incorporating Ni-NW nanomaterial prepared with the low Ru concentration, Ru(L)@Ni-

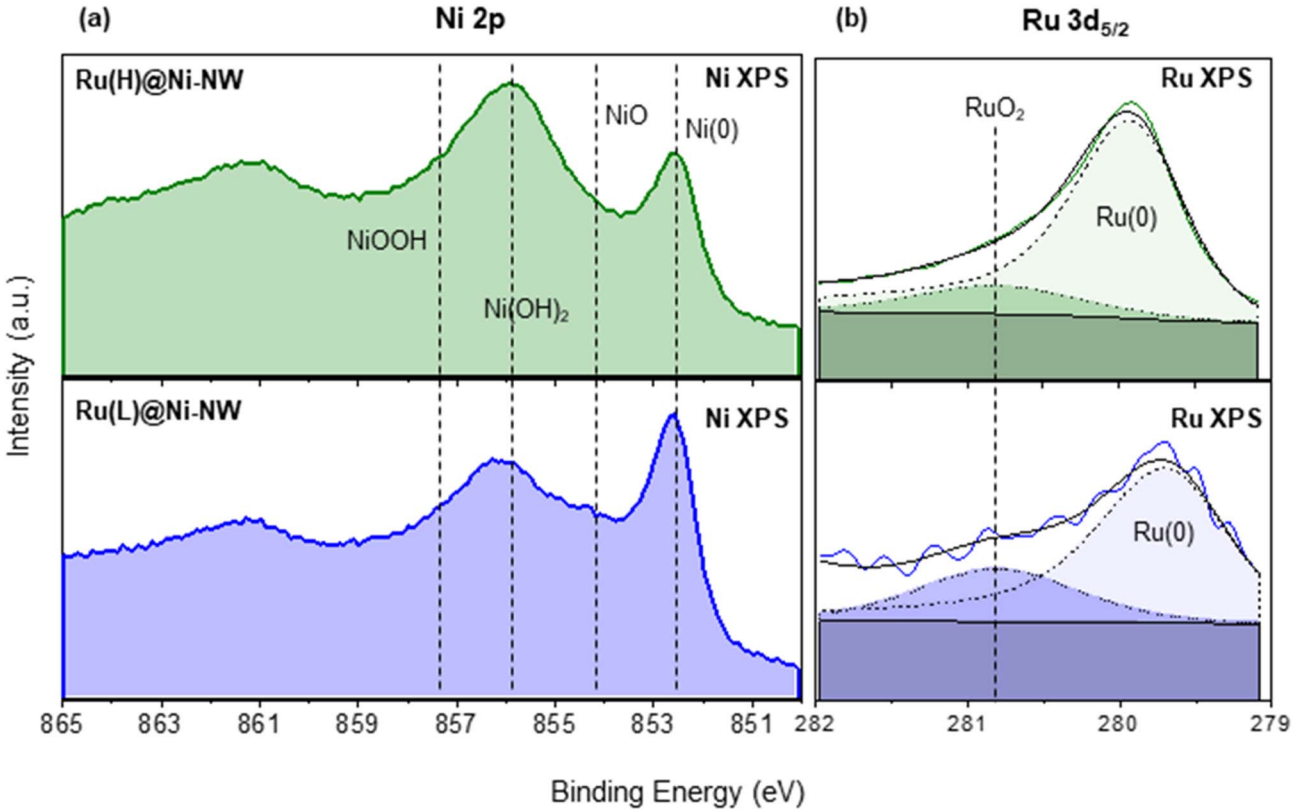

Fig. 2 Ni $2p_{3/2}$ XPS spectra of Ru(L)@Ni-NW (blue) and Ru(H)@Ni-NW (green) (a). Ru $3d_{5/2}$ XPS spectra of Ru(L)@Ni-NW (blue) and Ru(H)@Ni-NW (green) (b). Metallic-Ru component (Ru $3d_{5/2}$ 279.7–280.3 eV, dashed black), RuO_2-component (Ru $3d_{5/2}$ 280.8 eV, dotted black), and envelope (bold black).

NW, did not show the presence of Ru NPs, that of the nanomaterial prepared with high Ru incorporation, Ru(H)@Ni-NW, clearly showed the presence of Ru NPs (Fig. S2 and 1f).

3.2.2. ICP-OES and PXRD analysis. The presence of Ru was confirmed by ICP-OES and PXRD analyses for the two nanomaterials, Ru(L)@Ni-NW and Ru(H)@Ni-NW. ICP-OES provided a Ru content of 0.43 % wt and 3.2 % wt for Ru(L)@Ni-NW and Ru(H)@Ni-NW, respectively. The crystallinity and phase purity of the nanomaterials were examined by PXRD for Ru(L)@Ni-NW and Ru(H)@Ni-NW (Fig. S3) and compared to those of the native Ni-NWs.[31] The PXRD patterns indicated the presence of Ni(111), Ni(002) and Ni(022) peaks, attributed to the Ni face centered cubic (fcc) structure (Ni-ICDD: 96-901-2978), thus confirming the metallic state of Ni in all nanomaterials. Also, the PXRD pattern of Ru(L)@Ni-NW revealed the presence of only very small peaks that can be attributed to Ru in the form of a poorly crystallized or even amorphous phase (Fig. S3a). In contrast, the PXRD pattern of Ru(H)@Ni-NW showed better-defined peaks corresponding to the Ru(010), Ru(002), Ru(012), Ru(110), Ru(013) and Ru(112) crystalline planes of the Ru hcp structure (Ru-ICDD-96-900-8514) (Fig. S3b). In addition, the size of individual Ru crystallites in Ru(H)@Ni-NW was calculated by using the Scherrer equation method to be *ca.* 7.6 nm.[49] The $Ni(OH)_2$ surface layer obtained after the air-passivation process is not observable in PXRD due to its amorphous nature, in accordance with a previous report on pristine Ni-NWs.[31] However, the presence of $Ni(OH)_2$ is detected by XPS, a surface sensitive technique, as will be discussed in the following section.

3.2.3. XPS analysis. XPS analysis allowed discerning the surrounding chemical environment and oxidation state of the Ni in the Ni-NWs and the Ni and Ru in the two Ru@Ni-NW nanomaterials. The Ni $2p_{3/2}$ XPS spectra of Ru(H)@Ni-NW (Fig. 2a, green trace) revealed the presence of two sharp peaks. The one centered at 852.6 eV is attributed to Ni(0) and the other peak could be deconvoluted into three peaks centered at ≈854.0 eV, ≈856.0 eV and ≈857.5 eV attributed to NiO, $Ni(OH)_2$ and NiO(OH), respectively.[50–52] Similar peaks were observed for the Ru(L)@Ni-NW nanomaterial (Fig. 3a, blue trace). These results confirmed the layered structure of the native Ni-NW nanomaterial that comprises a metallic Ni phase surrounded by a $Ni(OH)_2$/NiO(OH) shell.[31] Interestingly, no signal for $Ni(OH)_2$/NiO(OH) was visible in the XPS spectrum of the passivated Ni-NW nanomaterial, but only a signal corresponding to $Ni(OH)_2$ was visible.[31] Thus, its detection in the Ru@Ni-NW nanomaterials may arise from the presence of Ru that may help the stabilization of higher oxidation states of Ni (*i.e.* NiO(OH)), as otherwise described in NiRu alloys[53] and Ru-containing Ni hydrotalcite-type materials.[54]

XPS analysis in the Ru $3d_{5/2}$ region gave evidence of the presence of Ru in two different phases, namely metallic Ru (Ru(0)) and RuO_2. Indeed, the intense peak can be deconvoluted

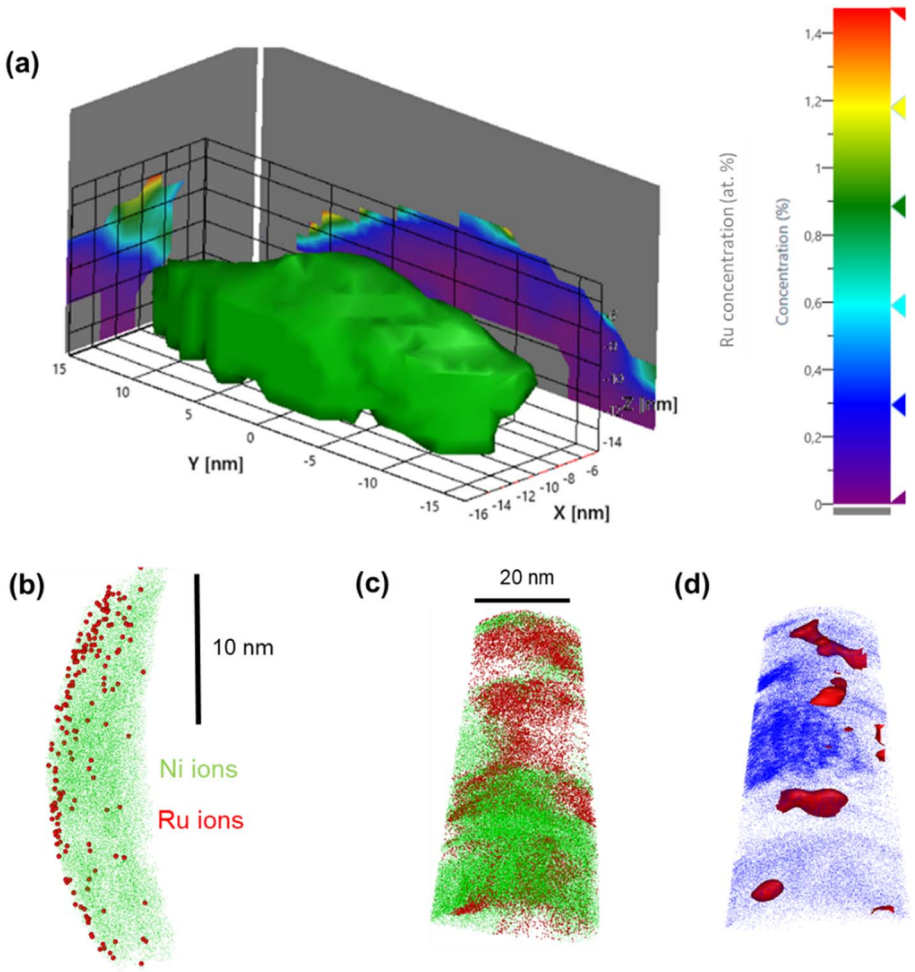

Fig. 3 APT reconstruction of a Ru(L)@Ni-NW segment: Ni iso-concentration surface delineating the 3-D NW segment structure along with the 2-D Ru concentration map projected on the x-y plane (a). 2-D Ni and Ru ion distribution; Ru ions are localized at the surface of the Ni-NW (b). APT reconstruction of a Ru(H)@Ni-NW segment: Ni (green) and Ru (red) ion distribution at the 3.2% Ru iso-concentration surface (red) (c) and along the APT specimen delineated by the Co embedding matrix (blue) (d).

into one component in the range of 279.7–280.3 eV (Ru(0)) and another one at 280.8 eV (RuO_2) (Fig. 2b).[55] Actually, and as expected after air exposure, the RuO_2 contribution can be attributed to the formation of a RuO_2 layer over the Ru(0) NPs.[43,56] Interestingly, as shown in Fig. 2b, the Ru(0) component in Ru(L)@Ni-NW (279.6 eV) appears at lower binding energies than for Ru(H)@Ni-NW (279.9 eV) and related Ru NPs reported by our group,[43,56,57] pointing at an effective interaction (electron transfer from Ni to Ru) between the two metals in the low Ru content system, analogously as described for NiRu alloys, where the electron donation from Ni to Ru provokes a negative shift (decrease in energy) of the Ru $3d_{5/2}$ peak.[53]

3.2.4 APT analysis. The high chemical sensitivity of APT measurements allowed the detection of small concentrations of Ru and their 3-D distribution along the Ni-NW nanomaterials. This was particularly important for the Ru(L)@Ni-NW nanomaterial due to its low concentration of Ru, which could be detected by APT, as shown in its representative mass spectrum (Fig. S4). To perform APT experiments, the nanomaterial was embedded in a Co matrix (see the experimental methods). The corresponding 3-D distribution of a segment from Ru(L)@Ni-NW within the Co matrix is visualized in Fig. 3. The detected Ru ions (red dots) are clearly distributed along the Ni–Co interface (Ni appears in green; Co distribution not shown) in Fig. 3b. This result indicates that the Ru ions are mainly located at the surface of the Ni-NWs. Due to the possible chromatic aberrations originating from the field evaporation behaviour of Ru in Ni-NWs, it is difficult to determine if Ru is forming small clusters or if it is distributed mostly as single atoms.[58] These aberrations mostly influence the spatial resolution along the *x*–*y* coordinate of the measurement,[59] thus affecting the accurate visualization of Ru atoms throughout the Ni-NW surface. Nonetheless, as observed in Fig. 3a, it is possible to quantify the Ru concentration within the Ni-NW and determine that the highest Ru concentrations are localized in the surface region of the Ni-NW nanomaterial (*ca.* 1.4 at%), in line with the low total concentration in the sample (*ca.* 0.13 at%).

In contrast, APT measurements of Ru(H)@Ni-NW showed a different Ru distribution along the Ni-NW surface. This is highlighted in Fig. 3c, where the higher concentration of Ru

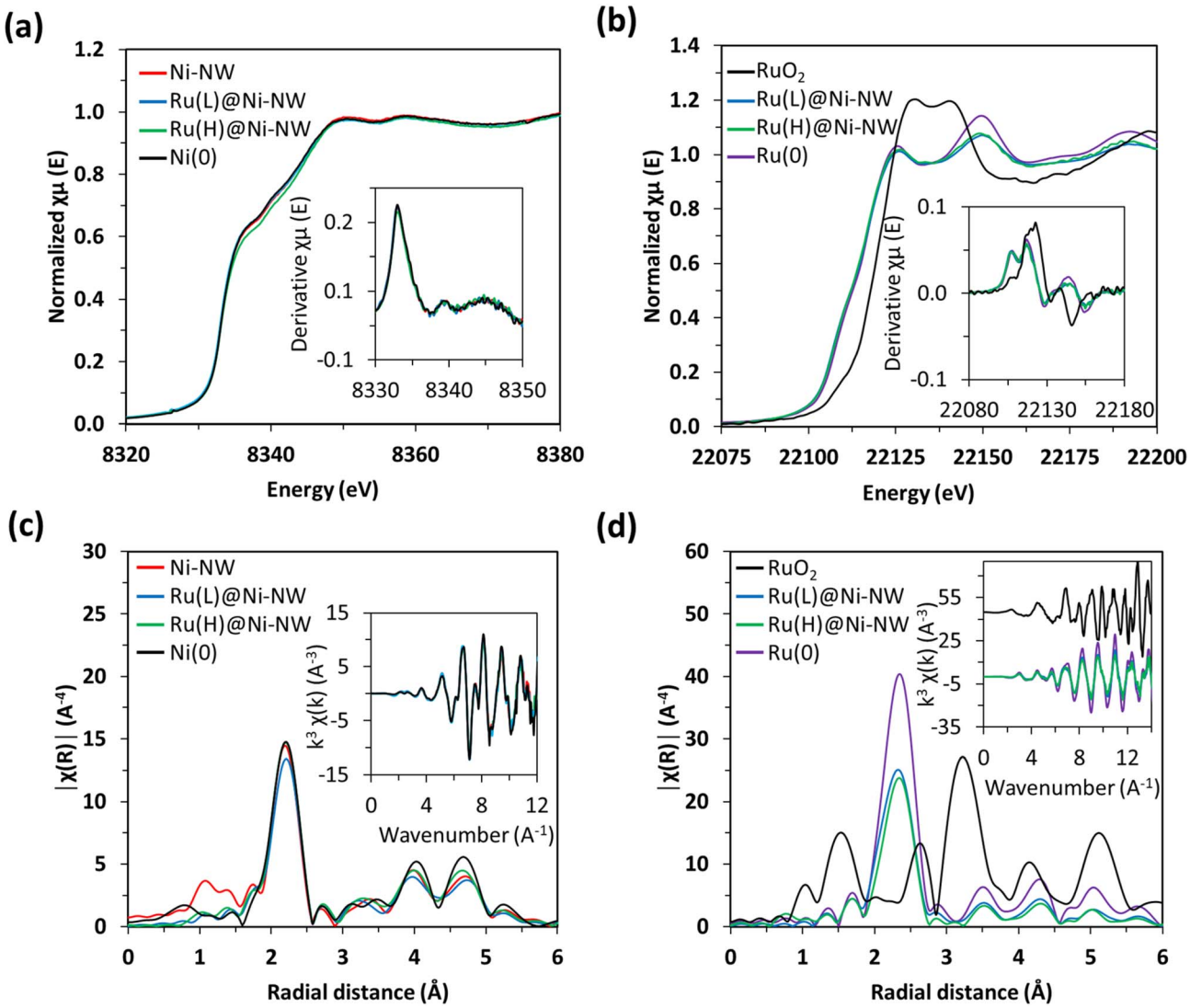

Fig. 4 Normalized Ni K-edge XANES for Ni-NW, Ru(L)@Ni-NW and Ru(H)@Ni-NW non-passivated nanomaterials and for the Ni(0) reference. Inset: the derivative of the Ni K-edge (a). Normalized Ru K-edge XANES for as-synthesized RuO_2, Ru(L)@Ni-NW and Ru(H)@Ni-NW, and the Ru(0) reference. Inset: the derivative of the Ru K-edge (b). Fourier transforms of k^3-weighted Ni EXAFS. Inset: EXAFS region $k^3\chi(k)$ for Ni systems together with a Ni(0) reference (c). Fourier transforms of k^3-weighted Ru EXAFS. Inset: EXAFS region $k^3\chi(k)$ for Ni systems together with Ru(0) and RuO_2 references (d).

appears as Ru agglomerates throughout the Ni-NW nanomaterial. An iso-concentration surface of the detected Ru ions (Fig. 3d) suggests that Ru is present in the form of NPs ranging from 5 to 10 nm in width, in concordance with the calculation of the crystallite sizes from PXRD analysis (Fig. S3b). The 3D reconstruction and Ru morphology seen in Fig. 3c are reminiscent of the results obtained by Rivas *et al.*,[60] who studied the embedding of Ru NPs in a Co matrix using APT. This result further confirms that there is a certain Ru concentration threshold during synthesis above which Ru NPs are formed rather than single atoms or small clusters at the surface of Ni-NWs.

3.2.5. XAS analysis. The electronic structure of the Ni and Ru elements in the non-passivated Ni-NW, Ru(L)@Ni-NW and Ru(H)@Ni-NW nanomaterials was investigated by X-ray absorption spectroscopy (XAS). These measurements were especially important to distinguish between the formation of small clusters or single atoms in the Ru(L)@Ni-NW nanomaterial, where the small size of the Ru species present prevented its structural characterization by other techniques. The Ni and Ru K-edges are sensitive to the oxidation state, the geometry and the coordination environment around the metal centers. As seen in Fig. 4a, the Ni K-edge X-ray absorption near edge structure showed the position of the edges for Ni-NWs, Ru(L)@Ni-NW and Ru(H)@Ni-NW at 8333 eV, which matches that of the Ni(0) reference, indicating that the three nanomaterials are mainly composed of metallic Ni, as expected for non-passivated nanomaterials. This result is in agreement with the extended X-ray absorption fine structure (EXAFS) region spectra (Fig. 4c), which are dominated by the presence of an intense feature characteristic of the Ni–Ni bonds at 2.49 Å and two additional low intensity peaks at longer distances, provoked by typical scattering with the nearest neighbors and the remote

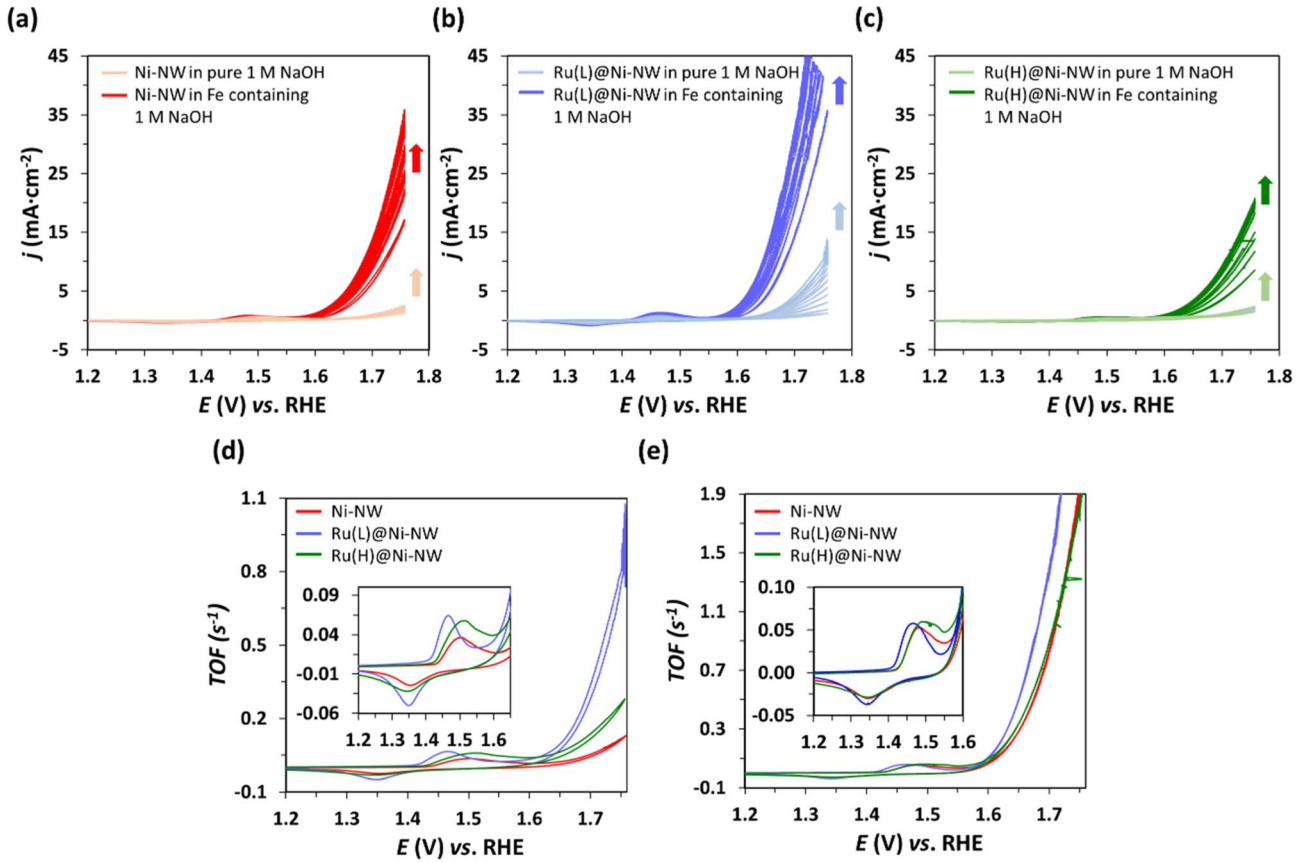

Fig. 5 Consecutive CV cycles performed at pH 14 in Fe-free (purified) 1 M NaOH (light colours) and, afterwards, in Fe-containing (non-purified) 1 M NaOH (dark colours) to assess the OER electrocatalytic activity of Ni-NWs (a), Ru(L)@Ni-NW (b) and Ru(H)@Ni-NW (c). Comparison of the last CV normalized by the calculated TOF (see the Experimental section for TOF calculation) of the different electrocatalysts in Fe-free (d) and Fe-containing (e) electrolyte.

Ni centers in the Ni(0) metallic structure, respectively (Fig. S5 and Table S2).

Similar findings were observed for the Ru signals in the Ru(L)@Ni-NW and Ru(H)@Ni-NW nanomaterials, where the XANES spectra and their derivatives are overlapped with the spectrum of metallic Ru(0) foil (Fig. 4b). The comparison with the RuO_2 reference spectrum shows that the presence of Ru(IV) in the whole Ru-incorporating Ni-NW materials is negligible, as expected for non-passivated nanomaterials. Furthermore, the *R*-space spectra showed the distinctive feature of Ru(0) attributed to the short Ru–Ru distance of 2.68 Å (Fig. 4d, S6 and Table S2). In fact, the EXAFS spectra perfectly overlap with that of Ru(0), suggesting the presence of small clusters or nanoparticles with well-resolved Ru–Ru scattering patterns rather than the Ru–Ni interactions expected for single-atom species. Focusing on the Ru(L)@Ni-NW nanomaterial, for which the presence of NPs was discarded in TEM images, this observation points to the presence of small (sub-nanometric) Ru clusters, not observable in low magnification electron microscopy images.

3.3. Electrocatalytic performance towards the OER in alkaline media

The catalytic activity of the passivated Ni-NWs, Ru(L)@Ni-NW and Ru(H)@Ni-NW nanomaterials was studied towards the OER at pH 14. First, 10 consecutive cyclic voltammetry (CV) cycles were performed from 1.05 V to 1.75 V *vs.* RHE in an Fe-free (see the Experimental section for further details) 1 M NaOH solution (Fig. 5). Second, the same electrodes were tested in an Fe-containing (non-purified) 1 M NaOH solution by performing another 10 consecutive CV cycles (Fig. 5).

As shown in Fig. 5, when scanned anodically up to 1.75 V *vs.* RHE, all electrodes showed one anodic peak in the oxidative forward scan prior to a sharp current increase assigned to the electrocatalytic OER. According to literature data,[61,62] the first faradaic process observed in the voltammograms (E_{ap} = *ca.* 1.5 V *vs.* RHE) could be attributed to the oxidation of Ni(II) to Ni(III), following eqn (1). The cathodic wave in the backward scan corresponds to the respective inverse reduction process of the NiO(OH) species.

$$Ni(OH)_2 + OH^- \leftrightarrow NiO(OH) + H_2O + e^- \quad (4)$$

The magnitude of this Ni(II)/Ni(III) redox wave (eqn (4)) is indicative of the number of Ni redox electroactive centers present in each electrode, and it has been used to estimate the TOF (s^{-1}) evolution *vs.* *E*, considering Ni as the active species[63] (Fig. 5d and e, see the Experimental section for further details). This enables the direct comparison of the electrochemical

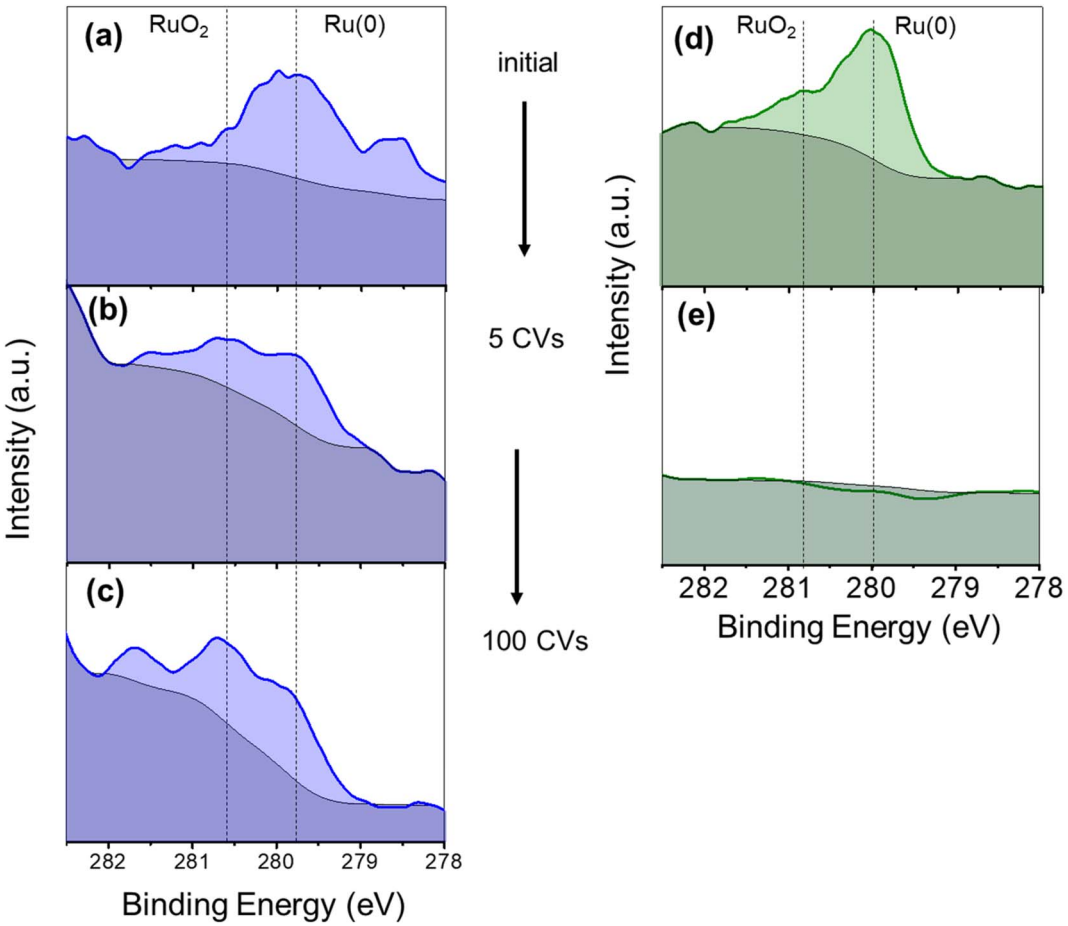

Fig. 6 Ru $3d_{5/2}$ XPS spectra (279.7–280.3 eV) on FTO electrodes of as prepared Ru(L)@Ni-NW (a), after 5 CV cycles (b) and after 100 CV cycles (c), and of as prepared Ru(H)@Ni-NW (d) after 5 CV cycles (e) at pH 14 in Fe-containing 1 M NaOH.

properties of the three nanomaterials studied despite the potential variation in the deposited amount of each electrocatalyst.

As can be observed in Fig. 5a–c there is an increase in j after 10 progressive CV cycles for all electrodes under both Fe-containing and Fe-free conditions. Interestingly, even when purified electrolyte (Fe-free) is employed, the three electrocatalysts activate, which may be due to their hydration and the Ni(0) oxidation.[64] It is important to highlight that, under these Fe-free conditions, the electrocatalyst presenting higher activation and superior performance is Ru(L)@Ni-NW (Fig. 5d), indicating that the presence of the sub-nanometric Ru clusters is beneficial for the intrinsic catalytic properties of the Ni nanomaterial. These results agree with the superior performance of Ru(L)@Ni-NM in the Fe-free electrolyte. When the same electrodes were then submerged in an Fe-containing (non-purified) electrolyte and 10 additional consecutive CV cycles were performed, the activity of the electrodes increased more than before, mostly due to Fe incorporation into the Ni structure, a common phenomenon observed in Ni-based electrocatalysts under OER conditions in alkaline media.[13] Due to the observed activation process, the overpotential needed to achieve the standard benchmarking current density of 10 mA cm^{-2} (η_{10}) has been extracted from the 10th CV cycle to compare the samples, the obtained values being 454 mV, 414 mV and 476 mV for Ni-NWs, Ru(L)@Ni-NW and Ru(H)@Ni-NW, respectively. These results highlight that the incorporation of 0.43 % wt of Ru in the Ni-NWs led to a better catalyst for the OER, but a higher loading of Ru (3.2 % wt) was not beneficial, as will be further discussed. To study any possible effect of the Ru incorporation on the ability of the nanomaterials to incorporate Fe, the Ni-NW, Ru(L)@Ni-NW and Ru(H)@Ni-NW nanomaterials were analysed by APT after Fe incorporation. The results (Fig. S7–S9) show the presence of similar amounts of Fe on the surface of the three nanomaterials, thus indicating that the observed differences in OER performance are not caused by the existence of either a higher or lower percentage of this element. These results agree with the superior performance of Ru(L)@Ni-NW in the Fe-free electrolyte.

The long-term stability has been evaluated for the best performing system Ru(L)@Ni-NW at 10 mA cm^{-2} for more than 19 h, showing no decrease in activity (SI Fig. S10 and S11). In addition, its stability at higher current densities (50 mA cm^{-2}) has also been assessed for 1 hour (Fig. S12 and S13), showing a slight increase in the overpotentials, pointing out the remarkable robustness of this nanomaterial under these demanding conditions.

Interestingly, the non-faradaic redox wave (eqn (4)) appearing before the catalytic process presented a shift in potential depending on the Ru content (insets in Fig. 5d and e). Ni-NWs and Ru(H)@Ni-NW presented their oxidation wave at 1.48 V *vs.* RHE in Fe-containing electrolyte and at 1.50 V *vs.* RHE in purified electrolyte. On the other hand, the Ni(II)/Ni(III) oxidation wave of Ru(L)@Ni-NW appears at 1.46 V *vs.* RHE in both electrolytes. This points that the Ru(L)@Ni-NW nanomaterial with 0.43 wt% Ru stabilizes higher oxidation states on the Ni-NWs.

3.4. XPS analysis after OER electrocatalysis

The evolution of the electrocatalysts during the activation process discussed above was analysed by XPS on the Ru(L)@Ni-NW and Ru(H)@Ni-NW electrodes after the first 5 CV cycles. As can be observed in Fig. 6a and d, initially both electrodes presented Ru(0) and RuO_2 characteristic signals, as described in Section 3.2.3. However, after only 5 CV cycles at pH 14 from the open circuit potential up to 1.75 V *vs.* RHE, the Ru $3d_{5/2}$ XPS signal disappeared from the Ru(H)@Ni-NW electrode (Fig. 6e), whilst it was still present in the Ru(L)@Ni-NW electrode (Fig. 6b). In the case of Ru(L)@Ni-NW, this signal remained even after 100 CV cycles under the same conditions (Fig. 6c). It is worth noticing that the ruthenium oxidation state of the Ru(L)@Ni-NW electrodes shifted from Ru(0) to RuO_2 as more CV cycles were run (Fig. 6a–c). The same oxidation tendency was found for the Ni metal centers (Fig. S14), where the signal of Ni(0) almost disappeared after only 5 CV cycles, indicating significant surface oxidation under operative conditions.

These experiments suggest a lack of stability under catalytic conditions for Ru(H)@Ni-NW, which contains Ru NPs of *ca.* 8 nm in size, in contrast to Ru(L)@Ni-NW, where the Ru is dispersed as small (sub-nanometric) clusters. This difference in stability between the Ru NPs and the sub-nanometric clusters can explain why the OER activity of Ru(H)@Ni-NW is similar to that of bare Ni-NWs, which do not contain Ru (Fig. 5).

To distinguish between potential and non-potential driven dissolution of the Ru NPs in Ru(H)@Ni-NW, an electrode containing this nanomaterial was immersed overnight into the non-purified 1 M NaOH electrolyte and its Ru $3d_{5/2}$ XPS spectrum was recorded. As shown in Fig. S15, the Ru XPS signal was still clearly visible after the long-time immersion, indicating the presence of the metal, which points to a potential driven process. The stability of RuO_2 anodes at high applied potentials was previously studied in the literature, concluding that the oxidation of RuO_2 leads to the formation of soluble RuO_4, RuO_4^- or RuO_4^{2-} species.[65–67]

3.5. UV-vis spectroelectrochemistry studies

In situ UV-vis spectroelectrochemistry has been used to track the changes and the accumulation of different species along a range of potentials for the three Ni-based nanomaterials.[68] The objective was to track the oxidation process from $Ni(OH)_2$ to NiO(OH) (eqn (4)) in Ni-NWs, Ru(L)@Ni-NW and Ru(H)@Ni-NW using pH 14 purified (Fe-free) and non-purified (Fe-containing) electrolytes after activation (10 consecutive CV cycles arriving at catalytic conditions, see Section 3.3 above and the Experimental section for further details).

The difference in absorbance (ΔO.D.) when applying a potential below and above the potentials where the Ni oxidative wave appears is shown in Fig. 7 for the purified electrolyte and in Fig. S10 for the Fe-containing one. The spectral features for Ni-NWs and Ru(H)@Ni-NW are similar, with a broad band peak centered at 450 nm characteristic of the NiO(OH) species according to the literature (Fig. 7a and c, S16a and c).[16,63] The observation of a similar electronic structure between activated Ni-NWs and Ni(H)@Ni-NW is in accordance with the post-electrocatalysis XPS results described above, demonstrating the loss of ruthenium after activation of the Ru(H)@Ni-NW nanomaterial. On the other hand, Ru(L)@Ni-NW presented a very different spectral pattern, with increasing absorption towards the NIR, peaking at 650 nm (Fig. 7b and S16b). This different spectral shape suggests that the presence of the small Ru clusters may change the electronic structure of the Ru(L)@Ni-NW nanomaterial.[41,43]

3.6. DFT calculations

With the aim of analyzing the influence of Ru-based sub-nanometric clusters on the $Ni(OH)_2$ to NiO(OH) oxidation

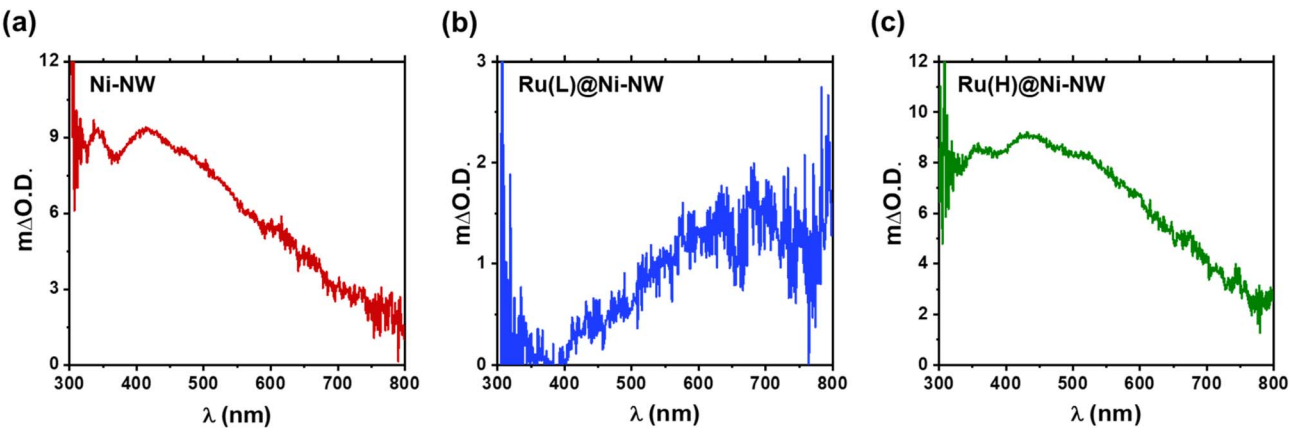

Fig. 7 ΔO.D. UV-vis absorption spectra of the species accumulated after the Ni(II)/Ni(III) redox wave before the catalytic region in pure 1 M NaOH and after activation (10 CV cycles up to catalytic potentials to stabilize the systems). Ni-NWs (a), Ru(L)@Ni-NW (b) and Ru(H)@Ni-NW (c).

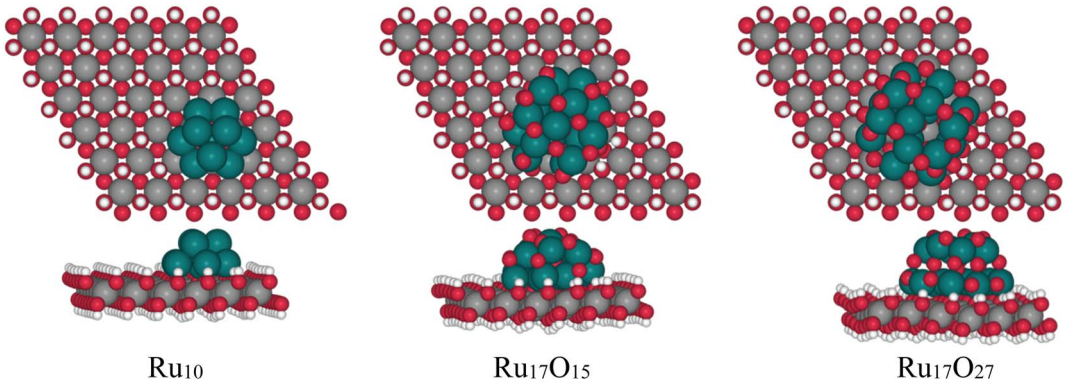

Fig. 8 Optimized structures of Ru_{10}, $Ru_{17}O_{15}$ and $Ru_{17}O_{27}$ clusters over a $Ni(OH_2)$ (100) layer.

process (eqn (4)), DFT (PBE-*U*-D3) calculations on the three model systems have been performed, as shown in Fig. 8. The models are based on either a Ru_{10}, $Ru_{17}O_{15}$ or $Ru_{17}O_{27}$ motif supported on a (6×6) $Ni(OH)_2$ monolayer supercell of the (001) surface in accordance with the sub-nanometric Ru clusters present on the Ru(L)@Ni-NW nanomaterial with consideration of different oxidation states of Ru (0, 1.8, and 3.2, respectively).

For each model, the exposed H atoms of $Ni(OH)_2$ have been classified as a function of the distance and position with respect to the Ru cluster (atoms in blue shades in Fig. 9). The energy cost of the proton coupled electron transfer (PCET) step associated with the transformation of *OH into *O + $1H^+$ + $1e^-$, assuming the computational standard hydrogen electrode approach, has been computed for all of them.[48] The nomenclature of the different OH groups was implemented in relation to the distance to the closest Ru atom of each cluster in a way that, within each model, A describes the OH group that is further away from the Ru cluster and E denotes the site that is the closest.

The computed potentials at which PCET takes place vary from −0.47 to 1.10 V, from 0.24 to 1.22 V and from 0.89 to 1.14 V for Ru_{10}, $Ru_{17}O_{15}$ and $Ru_{17}O_{27}$, respectively (Fig. 9). In general, the sites that are closer to the ruthenium cluster are oxidized at lower potentials than the ones that are further away. The only exceptions are the D sites of the $Ru_{17}O_{15}$ and $Ru_{17}O_{27}$ clusters. In these cases, the atom of the cluster that is closer to the nickel site is an oxygen (H···O = 2.3 Å). This favours a weak hydrogen bond interaction with a H atom of the initial $Ni(OH)_2$ surface, thus stabilizing its structure and making its oxidation marginally more challenging. For the Ru cluster with lower O content, several surface sites are oxidized very easily (C of Ru_{10} and C and E of $Ru_{17}O_{15}$). This is associated with a large reorganization of the Ni nanomaterial in which the oxygen that loses the proton is transferred to the Ru cluster, oxidizing it. This suggests that Ru in Ru_{10} and $Ru_{17}O_{15}$ would be more easily oxidized than $Ni(OH)_2$, in agreement with the experimental evidence that under catalytic conditions almost all Ru(0) is transformed into RuO_2 in Ru(L)@Ni-NW (Fig. 6, left). Consequently, comparison with experiments should be made with the $Ru_{17}O_{27}$ model. Remarkably, even in this case, the absolute values seem to be underestimated by almost 0.4 V when compared to the experimental results. However, DFT simulations usually reproduce relative energies of equivalent processes better than absolute values, and thus the focus is on the differences between sites. The oxidation of A, which is essentially not influenced by the presence of the Ru cluster (the shortest H···Ru distance is 5.6 Å), is computed to occur at 1.05 V. For sites B/C and E, that are closer to the RuO_X cluster than A, the potential required to oxidize the nickel centre decreases by 0.04 V and 0.16 V, respectively. In fact, the closer the site is to the cluster, the lower is the potential required to oxidize the nickel center. Remarkably, the substitution of one Ni surface center by Fe has little effect on the Ni^{2+}/Ni^{3+} oxidation process (Fig. S17). Regardless of the considered H site, the oxidation of Ni becomes more demanding by 0.05–0.08 V. Moreover, the H sites closer to the $Ru_{17}O_{27}$ cluster are more easily oxidized than those that are far apart from the NPs. The only exception is the closest H site to Fe that implies the oxidation of iron. Overall, calculations suggest that the presence of the RuO_X clusters on $Ni(OH)_2$ tend to favour nickel oxidation, regardless of the presence or absence of Fe,

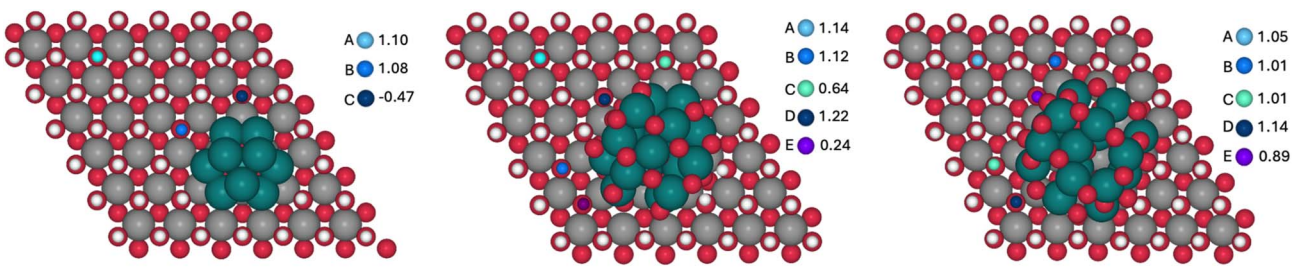

Fig. 9 OH sites considered for the $Ni(OH)_2$ oxidation in Ru_{10} (left), $Ru_{17}O_{15}$ (center) and $Ru_{17}O_{27}$ (right) model clusters and the corresponding computed potentials in V *vs.* RHE.

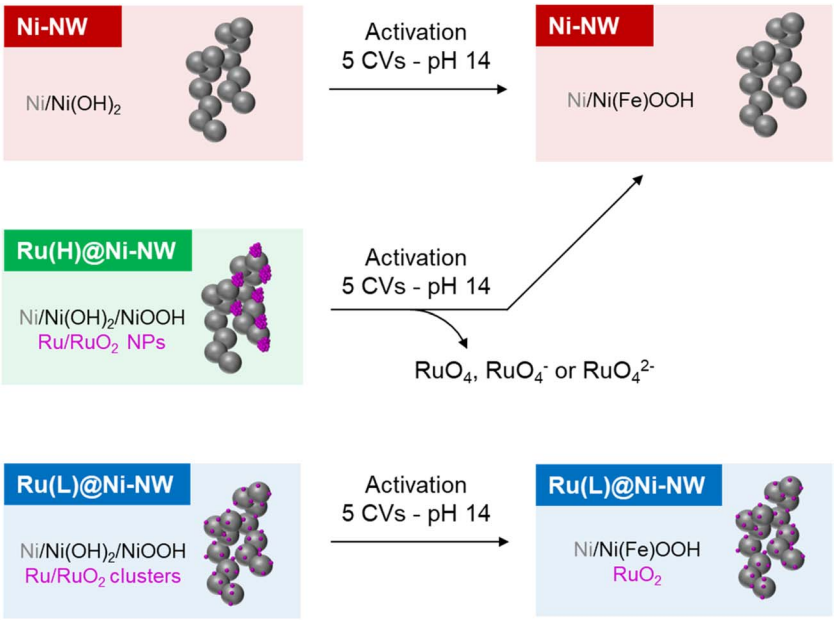

Scheme 2 Schematic representation of the main processes described in this work.

with a few exceptions related to very particular local environments. This agrees with the experimental data and further supports the relevance of the sub-nanometric Ru clusters incorporated on Ni-NWs to improve the OER electrocatalytic performance.

4. Summary

In this work we have prepared and characterized four different Ni-based electrocatalysts, Ni-NWs, Ru(L)@Ni-NW, Ru(H)@Ni-NW and Ru(HH)@Ni-NW. After passivation in open air, the pristine Ni-NWs can be considered a core–shell structure where a thin layer of $Ni(OH)_2$ covering the Ni(0) core, as evidenced by the surface sensitive XPS technique, whilst PXRD could only detect the presence of Ni(0).

The pristine Ni-NWs were modified with three different concentrations (0.43 % wt, 3.2 % wt and 6.4 % wt) of ruthenium, leading to Ru(L)@Ni-NW, Ru(H)@Ni-NW and Ru(HH)@Ni-NW, respectively. Both Ru(H)@Ni-NW and Ru(HH)@Ni-NW contain Ru NPs of *ca.* 8 nm on the Ni-NW surface. Therefore, only Ru(H)@Ni-NW was further studied. The Ru present in Ru(H)@Ni-NW was found to be unstable under catalytic OER conditions (Scheme 2). The similar ΔO.D. spectra obtained for both the bare Ni-NW and the Ru(H)@Ni-NW nanomaterials and the absence of the Ru signal in the post-catalysis (after 5 CV cycles) XPS spectrum of Ru(H)@Ni-NW evidence the absence of Ru shortly after the OER turnover starts. According to the literature, this can be attributed to the formation of soluble RuO_4, RuO_4^- or RuO_4^{2-} species, which was reported under similar oxidative conditions.[65–67]

On the other hand, Ru(L)@Ni-NW displays highly dispersed Ru all over the Ni-NW surface, as observed by EDX mapping and APT measurements (Scheme 2). This Ru is in the form of sub-nanometric clusters, as indicated by the presence of Ru–Ru interactions in the EXAFS results and the impossibility to observe them by HAADF-STEM due to their small size. The fine interaction between the Ru clusters and the Ni-NW surface directly impacts (i) the longer stability (>100 CV cycles) of the incorporated Ru at the Ni-NW surface under OER turnover conditions (Fig. 6) and (ii) the stabilization of high Ni oxidation states, which have been found to be more stable in the presence of Ru, as indicated by the shift in the Ni(II)/Ni(III) (eqn (4)) redox wave to lower potentials. The latter is further supported by spectroelectrochemical experiments (Fig. 7) that suggest a change in the electronic structure of Ru(L)@Ni-NW compared to its Ru-free Ni-NW counterpart. The earlier accumulation of higher oxidation states observed by electrochemical experiments for this Ru cluster-incorporating nanomaterial was also supported by DFT calculations, where the oxidation of Ni sites gradually increases as they approach the incorporated Ru. Interestingly, these observations are not dependent on the presence or absence of Fe in the nanomaterials. Thus, the Ru-induced stabilization of higher oxidation states in Ru(L)@Ni-NW is the main reason behind the enhanced OER performance observed in this nanomaterial.[41]

5. Conclusions

This work demonstrates that small variations in the concentration of incorporated Ru in a $Ni(OH)_2$/NiO(OH) electrocatalyst significantly impact its OER performance. This effect arises from differences in the structure and distribution of Ru atoms at the surface of the pristine Ni nanomaterial (Ni-NWs). At a high Ru concentration (Ru(H)@Ni-NW), Ru forms 8 nm NPs on the Ni-NW surface. Under catalytic oxidative conditions, the Ru NPs leach from the Ni-NW nanomaterial, as indicated by the absence of Ru-related peaks in post-reaction XPS analysis. Consequently, the activity of the Ru(H)@Ni-NW electrocatalyst

becomes comparable to that of bare Ni-NWs. In contrast, at a low Ru concentration (Ru(L)@Ni-NW), Ru forms well-dispersed sub-nanometric clusters, facilitating a strong interaction between the Ru and Ni atoms. This interaction stabilizes higher Ni oxidation states, as evidenced by electrochemical experiments and DFT calculations, and provokes changes in the electronic structure of the Ru(L)@Ni-NW nanomaterial, which shows enhanced OER performance. These data point out the importance of controlling the morphology of this incorporated Ru onto Ni-based electrocatalysts, which influences the interaction between the two metals and critically determines both the system stability and kinetics in the OER. Therefore, this work will contribute to paving the way to a rational design of efficient Ru-incorporating Ni-based OER electrocatalysts.

Conflicts of interest

There are no conflicts to declare.

Data availability

The data supporting this article have been included as part of the supplementary information (SI). Supplementary information is available. See DOI: https://doi.org/10.1039/d5ta08099a.

Acknowledgements

M. G. S. acknowledges funding from the HORIZON-MSCA-2021-PF-01 A-Trusol project No. 101063820. L. F. thanks MICIU/AEI/10.13039/501100011033 and FEDER, EU (PID2021-128197NA-I00) and El FSE invierte en tu futuro (RYC2018-025394-I Fellowship). X. S. and J. G.-A. thank MINECO/FEDER (PID2019-104171RB-I00) and MICIU (PID2023-146787OB-I00) for financial support. L. R. S. and X. S. M. (PID2023-151738NB-I00) thank MICIU for financial support. AGAUR is gratefully acknowledged for financial support (CLIMA2023-00036). CNRS, University of Toulouse Paul Sabatier and the Centre de Microcaractérisation R. Castaing (UAR 3623) are acknowledged for funding and access to scientific platforms. ANR PRECINANOMAT (project no. ANR-17-CE06-0017-01) is gratefully acknowledged for financial support (L. P.'s salary). AGM is thankful for Grant RYC2021 – 033479. XAS experiments were performed at the CLAESS beamline at the ALBA Synchrotron under proposal No. 2021095409 with the collaboration of ALBA staff. We especially acknowledge G. Gorni (CLAESS at ALBA) for his collaboration during the XAS experiments. AGM is thankful for Grant RYC2021 – 033479. C. S. acknowledges financial support from the Federal Ministry for Economic Affairs and Climate Action (BMWi) based on a decision taken by the German Bundestag.

References

1 N. S. Lewis and D. G. Nocera, *Proc. Natl. Acad. Sci. U. S. A.*, 2006, **103**, 15729–15735.
2 S. Yin Tee, K. Yin Win, W. Siang Teo, L.-D. Koh, S. Liu, C. Peng Teng, M.-Y. Han, S. Y. Tee, K. Y. Win, L. Koh, S. Liu, C. P. Teng, M. Han and W. S. Teo, *Adv. Sci.*, 2017, **4**, 1600337.
3 Z. Abdin, A. Zafaranloo, A. Rafiee, W. Mérida, W. Lipiński and K. R. Khalilpour, *Renewable Sustainable Energy Rev.*, 2020, **120**, 109620.
4 H. Inoue, T. Shimada, Y. Kou, Y. Nabetani, D. Masui, S. Takagi and H. Tachibana, *ChemSusChem*, 2011, **4**, 173–179.
5 C. R. Lhermitte and K. Sivula, *ACS Catal.*, 2019, **9**, 2007–2017.
6 L. Trotochaud, S. L. Young, J. K. Ranney and S. W. Boettcher, *J. Am. Chem. Soc.*, 2014, **136**, 6744–6753.
7 D. Friebel, M. W. Louie, M. Bajdich, K. E. Sanwald, Y. Cai, A. M. Wise, M. J. Cheng, D. Sokaras, T. C. Weng, R. Alonso-Mori, R. C. Davis, J. R. Bargar, J. K. Nørskov, A. Nilsson and A. T. Bell, *J. Am. Chem. Soc.*, 2015, **137**, 1305–1313.
8 S. Chen, Z. Kang, X. Zhang, J. Xie, H. Wang, W. Shao, X. Zheng, W. Yan, B. Pan and Y. Xie, *ACS Cent. Sci.*, 2017, **3**, 1221–1227.
9 M. A. Oliver-Tolentino, J. Vázquez-Samperio, A. Manzo-Robledo, R. D. G. González-Huerta, J. L. Flores-Moreno, D. Ramírez-Rosales and A. Guzmán-Vargas, *J. Phys. Chem. C*, 2014, **118**, 22432–22438.
10 N. Li, D. K. Bediako, R. G. Hadt, D. Hayes, T. J. Kempa, F. Von Cube, D. C. Bell, L. X. Chen and D. G. Nocera, *Proc. Natl. Acad. Sci. U. S. A.*, 2017, **114**, 1486–1491.
11 H. Xiao, H. Shin and W. A. Goddard, *Proc. Natl. Acad. Sci. U.S.A.*, 2018, **115**, 5872–5877.
12 N. Clament Sagaya Selvam, S. J. Kwak, G. H. Choi, M. J. Oh, H. Kim, W. S. Yoon, W. B. Lee and P. J. Yoo, *ACS Energy Lett.*, 2021, **6**, 4345–4354.
13 L. Trotochaud, S. L. Young, J. K. Ranney and S. W. Boettcher, *J. Am. Chem. Soc.*, 2014, **136**, 6744–6753.
14 L. Trotochaud, J. K. Ranney, K. N. Williams and S. W. Boettcher, *J. Am. Chem. Soc.*, 2012, **134**, 17253–17261.
15 S. Anantharaj, S. Kundu and S. Noda, *Nano Energy*, 2021, **80**, 105514.
16 M. Gorlin, J. F. De Araujo, H. Schmies, D. Bernsmeier, S. Dresp, M. Gliech, Z. Jusys, P. Chernev, R. Kraehnert, H. Dau and P. Strasser, *J. Am. Chem. Soc.*, 2017, **139**, 2070–2082.
17 B. J. Trześniewski, O. Diaz-Morales, D. A. Vermaas, A. Longo, W. Bras, M. T. M. Koper and W. A. Smith, *J. Am. Chem. Soc.*, 2015, **137**, 15112–15121.
18 M. Görlin, P. Chernev, J. F. De Araújo, T. Reier, S. Dresp, B. Paul, R. Krähnert, H. Dau and P. Strasser, *J. Am. Chem. Soc.*, 2016, **138**, 5603–5614.
19 G. Młynarek, M. Paszkiewicz and A. Radniecka, *J. Appl. Electrochem.*, 1984, **14**, 145–149.
20 E. S. Da Silva, A. Macili, R. Bofill, J. García-Antón, X. Sala and L. Francàs, *Chem.–Eur. J.*, 2024, **30**, e202302251.
21 H. Zhang, Y. Lv, C. Chen, C. Lv, X. Wu, J. Guo and D. Jia, *Appl. Catal., B*, 2021, **298**, 120611.
22 P. Zhai, M. Xia, Y. Wu, G. Zhang, J. Gao, B. Zhang, S. Cao, Y. Zhang, Z. Li, Z. Fan, C. Wang, X. Zhang, J. T. Miller, L. Sun and J. Hou, *Nat. Commun.*, 2021, **12**, 1–11.
23 M. Li, H. Wang, W. Zhu, W. Li, C. Wang, X. Lu, M. Li, W. Zhu, W. Li, C. Wang, X. G. Lu Alan MacDiarmid and H. Wang, *Adv. Sci.*, 2020, **7**, 1901833.

24 Z. Liu, M. Zha, Q. Wang, G. Hu and L. Feng, *Chem. Commun.*, 2020, **56**, 2352–2355.
25 D. Kim, S. Park, J. Choi, Y. Piao, L. Yoon, S. Lee, D. Kim, L. Y. S. Lee, S. Park, Y. Piao and J. Choi, *Small*, 2024, **20**, 2304822.
26 J. Liu, Y. Zheng, Y. Jiao, Z. Wang, Z. Lu, A. Vasileff and S. Z. Qiao, *Small*, 2018, **14**, 1704073.
27 I. C. Man, H. Y. Su, F. Calle-Vallejo, H. A. Hansen, J. I. Martínez, N. G. Inoglu, J. Kitchin, T. F. Jaramillo, J. K. Nørskov and J. Rossmeisl, *ChemCatChem*, 2011, **3**, 1159–1165.
28 Q. Sun, K. Reuter and M. Scheffler, *Phys. Rev. B: Condens. Matter Mater. Phys.*, 2003, **67**, 205424.
29 Y. D. Kim, A. P. Seitsonen, S. Wendt, J. Wang, C. Fan, K. Jacobi, H. Over and G. Ertl, *J. Phys. Chem. B*, 2001, **105**, 3752–3758.
30 C. Amiens, B. Chaudret, D. Ciuculescu-Pradines, V. Collière, K. Fajerwerg, P. Fau, M. Kahn, A. Maisonnat, K. Soulantica and K. Philippot, *New J. Chem.*, 2013, **37**, 3374–3401.
31 X. P. Fu, L. Peres, J. Esvan, C. Amiens, K. Philippot and N. Yan, *Nanoscale*, 2021, **13**, 8931–8939.
32 S. H. Kim, P. W. Kang, O. O. Park, J. B. Seol, J. P. Ahn, J. Y. Lee and P. P. Choi, *Ultramicroscopy*, 2018, **190**, 30–38.
33 B. Ravel and M. Newville, *J. Synchrotron Rad.*, 2005, **12**, 537–541.
34 D. González, B. Camino, J. Heras-Domingo, A. Rimola, L. Rodríguez-Santiago, X. Solans-Monfort and M. Sodupe, *J. Phys. Chem. C*, 2020, **124**, 1227–1237.
35 J. P. Perdew, K. Burke and M. Ernzerhof, *Phys. Rev. Lett.*, 1997, **78**, 1396.
36 G. Kresse and J. Furthmüller, *Phys. Rev. B: Condens. Matter Mater. Phys.*, 1996, **54**, 11169–11186.
37 G. Kresse and J. Hafner, *Phys. Rev. B: Condens. Matter Mater. Phys.*, 1993, **47**, 558–561.
38 S. L. Dudarev, G. A. Botton, S. Y. Savrasov, C. J. Humphreys and A. P. Sutton, *Phys. Rev. B: Condens. Matter Mater. Phys.*, 1998, **57**, 1505–1509.
39 Y. F. Li and A. Selloni, *ACS Catal.*, 2014, **4**, 1148–1153.
40 S. Grimme, J. Antony, S. Ehrlich and H. Krieg, *J. Chem. Phys.*, 2010, **132**, 154104.
41 P. E. Blöchl, *Phys. Rev. B: Condens. Matter Mater. Phys.*, 1994, **50**, 17953–17979.
42 G. Kresse and D. Joubert, *Phys. Rev. B: Condens. Matter Mater. Phys.*, 1999, **59**, 1758–1775.
43 N. Romero, D. A. Fenoll, L. Gil, S. Campos, J. Creus, G. Martí, J. Heras-Domingo, V. Collière, C. A. Mesa, S. Giménez, L. Francàs, L. Rodríguez-Santiago, X. Solans-Monfort, M. Sodupe, R. Bofill, K. Philippot, J. García-Antón and X. Sala, *Inorg. Chem. Front.*, 2023, **10**, 5885–5896.
44 D. A. Fenoll, M. Sodupe and X. Solans-Monfort, *Catal. Today*, 2024, **442**, 114908.
45 D. González, M. Sodupe, L. Rodríguez-Santiago and X. Solans-Monfort, *J. Catal.*, 2022, **412**, 78–86.
46 D. González, M. Sodupe, L. Rodríguez-Santiago and X. Solans-Monfort, *Nanoscale*, 2021, **13**, 14480–14489.
47 K. Mathew, R. Sundararaman, K. Letchworth-Weaver, T. A. Arias and R. G. Hennig, *J. Chem. Phys.*, 2014, **140**, 084106, DOI: 10.1063/1.4865107/1003843.
48 J. K. Nørskov, J. Rossmeisl, A. Logadottir, L. Lindqvist, J. R. Kitchin, T. Bligaard and H. Jónsson, *J. Phys. Chem. B*, 2004, **108**, 17886–17892.
49 A. L. Patterson, *Phys. Rev.*, 1939, **56**, 978.
50 M. C. Biesinger, B. P. Payne, L. W. M. Lau, A. Gerson and R. S. C. Smart, *Surf. Interface Anal.*, 2009, **41**, 324–332.
51 N. Weidler, J. Schuch, F. Knaus, P. Stenner, S. Hoch, A. Maljusch, R. Schäfer, B. Kaiser and W. Jaegermann, *J. Phys. Chem. C*, 2017, **121**, 6455–6463.
52 L. Zhu, T. Zheng, J. Zheng, C. Yu, N. Zhang, Q. Zhou, W. Zhang and B. H. Chen, *CrystEngComm*, 2018, **20**, 113–121.
53 Y. Zhou, Y. Liu, H. Tang and B. L. Lin, *J. Mater. Chem. A*, 2023, **11**, 10720–10726.
54 S. A. Sreenavya, B. T. Baskaran, G. V. Ganesh, S. D. Sharma, N. Kulal and S. A. Sakthivel, *RSC Adv.*, 2018, **8**, 25248–25257.
55 D. J. Morgan, *Surf. Interface Anal.*, 2015, **47**, 1072–1079.
56 J. Creus, S. Drouet, S. Suriñach, P. Lecante, V. Collière, R. Poteau, K. Philippot, J. García-Antón and X. Sala, *ACS Catal.*, 2018, **8**, 11094–11102.
57 J. Creus, L. Mallón, N. Romero, R. Bofill, A. Moya, J. L. G. Fierro, R. Mas-Ballesté, X. Sala, K. Philippot and J. García-Antón, *Eur. J. Inorg. Chem.*, 2019, **12**, 2071–2077.
58 E. A. Marquis and F. Vurpillot, *Microsc. Microanal.*, 2008, **14**, 561–570.
59 B. Gault, M. P. Moody, J. M. Cairney and S. P. Ringer, *Mater. Today*, 2012, **15**, 378–386.
60 N. A. R. Rivas, A. G. Manjón, M. Vega-Paredes, S. H. Kim, B. Gault, H. Jun, C. Jung, V. Berova, K. Hengge, T. Jurzinsky and C. Scheu, *Ultramicroscopy*, 2023, **254**, 113831.
61 M. W. Louie and A. T. Bell, *J. Am. Chem. Soc.*, 2013, **135**, 12329–12337.
62 Y. Gao, H. Li and G. Yang, *Cryst. Growth Des.*, 2015, **15**, 4475–4483.
63 L. Francàs, S. Corby, S. Selim, D. Lee, C. A. Mesa, R. Godin, E. Pastor, I. E. L. Stephens, K. S. Choi and J. R. Durrant, *Nat. Commun.*, 2019, **10**, 1–10.
64 S. Corby, M.-G. Tecedor, S. Tengeler, C. Steinert, B. Moss, C. A. Mesa, H. F. Heiba, A. A. Wilson, B. Kaiser, W. Jaegermann, L. Francàs, S. Gimenez and J. R. Durrant, *Sustainable Energy Fuels*, 2020, **4**, 5024–5030.
65 F. Hess, *Curr. Opin. Electrochem.*, 2023, **41**, 101349.
66 W. Li, C. Wang and X. Lu, *Nano Lett.*, 2024, **24**, 11779–11792.
67 G. Chen, Y. Zhu, S. She, Z. Lin, H. Sun and H. Huang, *InfoMat*, 2024, e12609.
68 C. A. Mesa, E. Pastor and L. Francàs, *Curr. Opin. Electrochem.*, 2022, **35**, 101098.

